Macromolecules

pubs.acs.org/Macromolecules Article

Structural Characterization of Amphiphilic Conetworks in Selective and Nonselective Solvents Using ^{1}H NMR and SAXS

Lucas Löser,* Carolin Bunk, Reinhard Scholz, Michael Lang, Frank Böhme, and Kay Saalwächter*

Cite This: https://doi.org/10.1021/acs.macromol.3c02139 Read Online

ACCESS | Metrics & More | Article Recommendations

ABSTRACT: We investigate the structural properties of model amphiphilic conetworks made by heterocomplementary end-linking of tetra-poly(ethylene glycol) tetra-poly(ϵ-caprolactone) PCL star polymers in selective and nonselective solvents using small-angle X-ray scattering, nuclear magnetic resonance (NMR) diffusometry, and double-quantum magic-angle spinning (DQ MAS) NMR techniques. The X-ray scattering experiments reveal the correlation lengths of our networks, including postcuring effects, and the microphase separation (MPS) of the networks swollen by a selective solvent, with cluster sizes independent of concentration. An estimation of hydrodynamic screening length as the length scale governing the diffusion process is achieved by monitoring the diffusion coefficients of polysaccharides and polystyrenes with different molecular weights. Furthermore, chemical-shift-resolved local chain mobilities in the microphase-separated system are observed using DQ MAS NMR, demonstrating immobilization of the linker end group and melt-like dynamics for clustered PCL chains, both of which are in qualitative agreement with bond-fluctuation Monte Carlo simulations of comparable model structures. Our analyses provide valuable insights into the structural properties and behavior of amphiphilic conetworks and the process of MPS under strong topological constraints, highlighting the effects of postcuring in a polymer network with star-shaped building blocks.

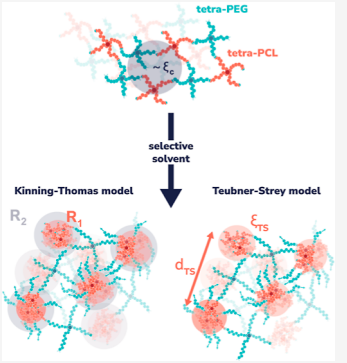

INTRODUCTION

The molecular transport of probes through swollen polymer networks is an important process deciding upon the usability and efficiency of these materials for many relevant applications in industries, such as usage for separation membranes, conductive layers in batteries, drug-release systems, or the design of scaffold systems for cell growth.[1−3] A special subclass of these materials are amphiphilic polymer networks (ACNs), which consist of a cross-linked set of hydrophilic and hydrophobic macromolecular precursors.[4−6] Due to their structure, they are uniquely suited to certain applications requiring, e.g., phase-specific molecular transport as needed in soft contact lenses,[7] drug delivery,[8] tissue engineering,[9] separation membranes,[10] and more.[11,12] Additionally, they are a potential candidate for polymer-based matrices in batteries.[13] Most of these applications rely on an efficient and controlled diffusion for a given system, which is especially needed for biomedical applications. An often used concept for describing the diffusion properties of a gel is the network mesh size, which dictates how freely a penetrant of a given size can move through the polymer network.[14−21] However, the accurate definition of the length scale corresponding to the term "mesh size" is not always clear, leaving significant space for speculation, spanning entire length scales from the geometrical mesh to the size of a chain correlation blob ξ_c. Nevertheless, the estimation of this length scale, especially for diffusion processes in new polymer materials, remains an important goal. In this work, all length scales are characterized in terms of either correlation length scales ξ_x or hydrodynamic blob sizes ξ_h.

A large variety of different characterization techniques can be geared to provide information on such challenging structures, including rather straightforward imaging techniques on the nm to μm scale such as scanning electron microscopy (SEM), transmission electron microscopy (TEM), and atomic force microscopy (AFM) as well as indirect methods such as conductivity measurements,[22] fluorescence recovery after photobleaching (FRAP),[23−25] and pulsed-field gradient-NMR (PFG NMR).[19,26−29] In contrast to conventional imaging methods, both FRAP and PFG NMR usually do not require potentially morphology-changing processing steps, and they are able to operate on real-life samples. Commonly, these methods require the presence of a probe molecule with a defined hydrodynamic size R_h as both methods analyze the change in the diffusion coefficient of probe molecules based on the ratio of R_h to ξ_h. As recently summarized in detail by Amsden,[30] various relevant parameters, such as chain stiffness, polymer−solvent interactions, interchain correlations, and the

Received: October 19, 2023
Revised: December 13, 2023
Accepted: December 15, 2023

interplay of obstruction vs free volume mechanisms, have been identified and fostered the discussion of different models. Notably, for probe molecules that are not colloids in the strict sense, additional caveats arise from the fact that the limiting length scale for linear chains will not be R_h but rather the hydrodynamic screening length ξ_h accessible from the transition from Zimm dynamics to Rouse dynamics.[31]

A well-established method for accessing length scales in swollen polymer systems is small-angle X-ray scattering (SAXS), which may allow for a noninvasive, probe-free exploration of the nanoscale morphology via probing differences in electron density on length scales ranging from 0.1 to 50 nm. Especially for the case of polymer gels, both the size of correlation blobs and potential solvent-induced microphase separation (MPS), if present, can be observed for some systems.[32−38] The actual relationship between the measured blob sizes and the structural morphology depends on the system and is not always readily accessible. Additional information is gained in the case of clustering systems as SAXS allows for the evaluation of length scales of MPS by applying appropriate fitting models such as, e.g., the one of Teubner and Strey (TS),[39] or suitable combinations of reasonable structure and form factors, like the combination of a Percus−Yevick hard-sphere structure factor with a sphere form factor.[40] This may allow for the estimation of the characteristic length scale and number of chains that can participate in the formation of clusters. Herein, both the aforementioned models are discussed and compared.

In the case of ACNs, the cross-linked network chains pose a constraint against rearrangements necessary to accommodate a selective solvent, hence it is of particular interest to compare correlation lengths in the swollen state both in good and selective solvents while also quantifying the length scale of MPS. It is not clear what the precise effects of a clustered phase on the overall morphology will be. However, a natural expectation for this process is a reduced degree of swelling that is accompanied by a larger osmotic pressure in the still swollen part that needs to be balanced by the network elasticity in some way. This process is expected to cause a change in the diffusivity of probe molecules in the swollen phase by reducing the volume accessible for the probes and changing the hydrodynamic screening length of the swollen phase.

So far, a variety of models and procedures provide length scales and aggregation numbers of these networks, but to our knowledge, none of these studies featured a critical comparison of different analysis models. Some works focus only on the inverse peak position as a rough (and potentially biased) measure for the interdomain distance,[33,41] whereas others assume, e.g., core−shell models that can be used to extract distances, radii, and aggregation numbers,[36−38,42] while correlation models yielding two approximate length scales are also used.[43,44]

A critical test of these models requires samples with a well-defined network structure. In this regard, different synthetic strategies of connecting precursors of similar or different philicities were used, including fast click reactions,[45] condensation reactions,[46,47] end-linking of small telechelic cross-linkers,[48] or the comparably slow heterocomplementary end-linking reaction using benzoxazinone-/amino-terminated tetra-arm star polymers.[49] In this work, we focus on our recently developed tetra poly(ethylene glycol) (PEG) - tetra-poly(ϵ-caprolactone) (PCL) amphiphilic conetwork (tPEG-tPCL ACN)[49] system that utilizes the latter synthesis approach, and we discuss the application and interplay of SAXS and PFG-NMR as tools for characterizing its structure and permeation properties. While initial correlations of topology−property relationships in good/common solvent have already been established and underpinned by theoretical work,[50] the changes in the topological properties of this system upon MPS under selective-solvent conditions (i.e., poor solvent for one of the components) will be addressed in this work for the first time. By measuring the diffusion coefficient of penetrants such as polysaccharides (PSCs) and polystyrene (PS) macromolecules, we estimate the respective microscopic length scales in the sense of a hydrodynamic screening length ξ_h (that we assume to be on the order of the correlation blob ξ_c in accordance with, e.g., ref 51), as well as in the microphase-separated state. These macroscopic properties will be compared to correlation lengths of the polymer network ξ_c, as estimated by SAXS. We show that the microphase-separated PCL domains of considerable size can still be formed despite the topological constraints of the network chains (see Figure 1 for a tentative sketch). We estimate the size and distance of the PCL domains in good agreement with computer simulation results, whose details are to be published separately. Our results yield insights into the diffusion and MPS behavior of ACNs while also providing a helpful methodological procedure for the analysis of PFG NMR data when working with samples showing no well-separated signals in their ^{1}H NMR spectrum, mostly due to the need of measuring inhomogeneous samples of undefined shape.

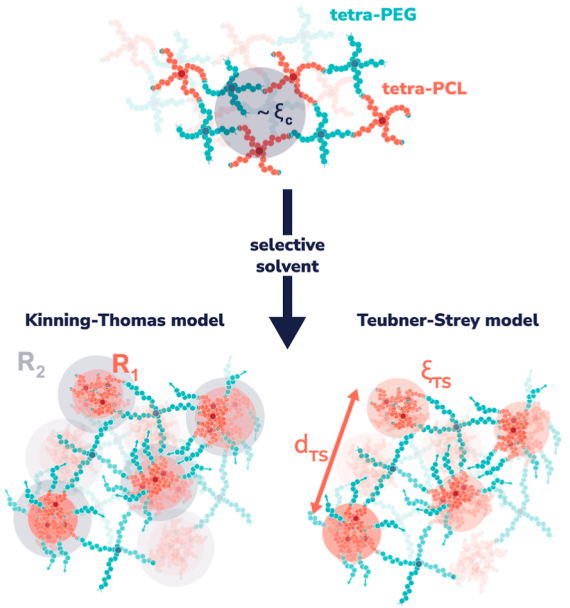

Figure 1. Tentative model picture of the MPS of our investigated tetra-poly(ethylene glycol) (PEG) tetra-poly(ϵ-caprolactone) (PCL) ACN as seen by the two respective models used for the SAXS data analysis. The Kinning−Thomas (KT) model (left) describes the morphology as hard spheres of radius R_1 with a soft repulsive corona of radius R_2, whereas the TS model yields information about the distance d_{TS} between the scatterers and a decay length scale ξ_{TS} of the real-space correlation function. Note that some chain ends are not drawn or only continued with an arrow for simplicity.

https://doi.org/10.1021/acs.macromol.3c02139
Macromolecules XXXX, XXX, XXX−XXX

EXPERIMENTAL SECTION

Sample Preparation. The tetra-arm star polymer networks investigated were synthesized based upon the protocol published in ref 49. Networks consist of either a combination of 10 kDa oxazinone-terminated tetra-arm star PCL and 10 kDa amino-terminated tetra-arm PEG or of 10 kDa oxazinone-terminated tetra-arm star PEG and 10 kDa amino-terminated tetra-arm PEG. Both the amphiphilic tetra-PEG−PCL and the nonamphiphilic tetra-PEG−PEG networks were prepared in the same manner (with only minor differences due to adjustments in stoichiometry to compensate for small differences in the molecular weight of the precursors) at different concentrations in toluene-d_8 as a common good solvent at T = 50 °C and a reaction time of t = 4 d. The networks are prepared at concentrations ranging from 35 to 350 g L^{-1} to be compared with the overlap concentration of 70 g L^{-1}.[49]

All probe molecules for diffusivity studies used in this work were purchased from Sigma-Aldrich and used as received. Concerning the diffusion of hydrophilic probe molecules, glucose (0.18 kDa) and dextran samples of different molecular weights (2.5, 6.0, 10, 20, 40, and 60 kDa) were used. For all experiments, the PSCs were dissolved in D_2O at a mass concentration of 50 mg mL^{-1} (5 wt %) and homogenized before each use to make sure that the compound is fully dissolved. The hydrophobic probe molecules consist of a set of gel permeation chromatography analytical standard PS samples with different molecular weights (1.0, 10, 30, 70, and 100 kDa). For all samples except the 1.0 kDa sample, a polydispersity index of ≤1.05 is given, with an exception being the 1.0 kDa sample, where the PDI is 1.13. Again, stock solutions at 50 g L^{-1} (5 wt %) in toluene-d_8 were prepared. Dried gels were swollen in solutions of D_2O and the respective PSCs, where they were swollen to equilibrium for at least 24 h each, reaching degrees of swelling of about $Q_{eq} \approx 4$. As gels swollen in toluene (+PS) reach a much higher equilibrium degree of swelling, a controlled degree of swelling of $Q = 5 \pm 0.5$ was achieved, which roughly matches the macroscopic swelling degree in the selective solvent. A volumetric degree of swelling is estimated based upon the change of mass of the sample by resorting to the following equation

$$Q_v = 1 + \left(\frac{\rho_p}{\rho_s}\right)\left(\frac{w_s}{w_p}\right) \tag{1}$$

Here, ρ_s is the solvent density, ρ_p is the polymer density (e.g., 1.13 g mL^{-1} for the average of PEG and PCL), and w_s and w_p are the respective masses of polymer and solvent used.

Methods. *Small-Angle X-ray Scattering.* SAXS experiments were performed using a retro-F laboratory setup (SAXSLAB) equipped with a microfocus X-ray source and an ASTIX multilayer X-ray optics as monochromator for Cu Kα radiation (λ = 0.154 nm). Measurements were recorded in vacuum (p < 1 mbar) using a PILATUS 3 R 300 K detector at two sample-to-detector distances (1 and 3 m) to cover both the SAXS and the wide-angle X-ray scattering (WAXS) regimes. All measurements were made at room temperature (~20 °C) and in transmission mode, where the transmission factor for all samples was between 20 and 50%.

For all scattering experiments, gels were either used as-prepared [in d_8-toluene and d_4-tetrahydrofuran (THF)] or dried in a vacuum oven (50 °C, 20 mbar) for 24 h and reswollen to equilibrium in D_2O. Afterward, the gels were carefully cut into small pieces (<2 mm × 2 mm × 2 mm) using a scalpel. The gel pieces were placed in a 2-piece screw-top hollow metal cylinder with a circular opening on both ends and a stiff poly(tetrafluoroethylene) (PTFE) O-Ring in between for ensuring isolation between the two screwable parts while not deforming the sample. The circular openings were sealed by mica plates with a thickness of 8−10 μm (purchased at SAXSLAB). This gastight setup prevents evaporation of solvent in the vacuum chamber of the SAXS setup while allowing for a 1 cm opening for the beam to traverse the sample with minimal influence from the setup itself. Any potential leaks would immediately be detected by eye as all samples would fully dry up within minutes of being exposed to the vacuum. Initial measurements of the sample holder with only mica plates without gel have shown no significant contribution in the SAXS regime but only sharp and easily identifiable peaks in the WAXS regime. *SAXSGUI* v2.19.02 was used for data reduction (azimuthal average) of the obtained SAXS data, while the postprocessing and evaluation of the reduced data relies on a basin-hopping algorithm (to reduce the chance of being trapped in a local optimization minimum) implemented in *Python* 3.09 and *LMFIT* 1.09.[52] The scattering curves obtained were automatically merged at about q = 0.1 $Å^{-1}$ based upon minimization of the average intensity difference in a small region around the merging point.

All SAXS curves obtained on measured PEG−PCL networks in both good and selective solvents include a specific characteristic superposition of signals. In a common good solvent, we have

$$I(q) = I_{bg} + I_{DB} + I_{OZ} \tag{2}$$

Here, I_{bg} denotes the incoherent background scattering intensity, I_{DB} is the Debye−Bueche function[53] describing the length scale Ξ of frozen concentration fluctuations, and I_{OZ} is an Ornstein−Zernike function[54] reflecting thermal fluctuations on a length scale ξ. The respective functions read as follows

$$I_{OZ} \approx \frac{1}{(1 + (q\xi_{OZ})^2)^{(1/2\nu)}} \tag{3}$$

$$I_{DB} = \frac{1}{(1 + [q\Xi]^2)^2} \tag{4}$$

Here, ν denotes the good solvent exponent and is taken to be ν = 0.588, resulting in an overall asymptomatic dependence of $q^{-1.7}$. It should be noted that the Debye−Bueche function can be substituted by, e.g., Porod's law as the low-q regime in our case only consists of a simple power-law function due to the lack of access to lower q. However, since the scattering data do not develop a plateau toward small q, alternate model functions for the frozen fluctuations like a Gaussian pair distribution cannot be used for data analysis.

In the case of MPS due to, e.g., a poor solvent for one of the components, these relations are extended to

$$I(q) = I_{bg} + I_P + I_{OZ} + I_{MPS} \tag{5}$$

where I_{MPS} is the additional contribution of the microphase-separated clusters arising from the collapse of the PCL phase (in case of water as a selective solvent) and I_P is Porod's law with d being the fractal dimension of the surface of the scatterers as follows

$$I_P(q) = I_0 \cdot q^{-(6-d)} \tag{6}$$

In the following, two different models were tested for fitting the additional contribution arising from the microphase separation. On the one hand, we evaluated the data using the popular TS model,[39] which is primarily used for liquid microemulsions with an average distance d of neighboring droplets and a decay length ξ. On the other hand, we tested an alternative method of Kinning and Thomas (KT),[40] who proposed a Percus−Yevick structure factor for hard spheres (core plus stretched, repulsive corona) in combination with a sphere form factor describing the scattering core to analyze SAXS data taken on micellar block copolymer structures in bulk. This model provides a defined core radius R_1 and the radius R_2 of a larger effective sphere comprising the core plus the outer "fluffy" shell. This model should in principle provide the same information as the TS model with the exception of also providing a volume fraction of effectively repulsive spheres. For both models, there exists experimental evidence that they can be used for the phase separation of polymer networks (e.g., refs 34, 42, 55−57) under certain conditions. Therefore, both will be used here, and the quantities obtained will be compared.

As noted, the KT model connects the form factor from spherical scattering entities P_{sphere} with a structure factor S_{PY} arising from their arrangement, for which the Percus−Yevick closure[58−60] is used

$$I(q) = S_{PY}(q, R_1, R_2, f)P_{sphere}(q, R_1) \tag{7}$$

https://doi.org/10.1021/acs.macromol.3c02139
Macromolecules XXXX, XXX, XXX−XXX

$$P_{\text{sphere}} = \frac{9\rho_0^2 v_0^2}{(qR_1)^6}[\sin(qR_1) - (qR_1)\cos(qR_1)]^2 \quad (8)$$

Here, f denotes the fraction of the effective hard spheres, ρ_0 is the scattering contrast, and v_0 corresponds to the sphere volume. For the rather complicated full equation of the structure factor S_{PY}, the reader is referred to ref 40. The original equation is modified so that not a single pair of radii R_1, R_2 is assumed, but rather a continuous log–normal distribution for the radius R_1 with an associated logarithmic (dimensionless) standard deviation σ, as presented, e.g., in ref 61. This is justified both from the experimental side (as one can clearly not observe the well-defined oscillations in the scattering curve, which are typical for P_{sphere}) and from the theoretical side, where in simulations on that specific system, it was found that the size distribution of the clusters is polydisperse besides an additional shape distribution of slightly ellipsoidal objects (to be published under separate cover). It is finally noted that in a selectively swollen ACN, being a 3-component system, scattering contrast may additionally arise within the swollen region having a separate, less swollen (more crowded) corona around the separated phase. This will be discussed below.

In the case of the TS model,[39] a nonparticulate and randomly distributed two-phase system with a well-defined interface is assumed, again neglecting potential contrast arising from concentration variations in the swollen phase. The system is modeled by a real-space correlation function that decays exponentially with a correlation length of ξ_{TS}, as described by the Debye–Bueche model.[53] Teubner and Strey modified this radially decaying pair correlation function by a radial oscillation in the following way

$$g(r) = \frac{d_{\text{TS}}}{2\pi r}\exp\left(-\frac{r}{\xi_{\text{TS}}}\right)\sin\frac{2\pi r}{d_{\text{TS}}} \quad (9)$$

Here, another length scale d_{TS} is introduced, which corresponds to the typical distance between the scattering moieties. Therefore, one obtains the following well-known equation for the observed scattering intensity

$$I(q) = \frac{1}{a_2 + c_1 q^2 + c_2 q^4} \quad (10)$$

where the coefficients a_2, c_1, and c_2 provide the real-space length scales d_{TS} (oscillation period; a measure of the distance between the center-of-mass for two clusters) and ξ_{TS} (decay length scale of the scattering moiety according to eq 9)

$$\xi_{\text{TS}} = \left[\frac{1}{2}\left(\frac{a_2}{c_2}\right)^{0.5} + \frac{1}{4}\left(\frac{c_1}{c_2}\right)\right]^{-0.5} \quad (11)$$

$$d_{\text{TS}} = 2\pi\left[\frac{1}{2}\left(\frac{a_2}{c_2}\right)^{0.5} - \frac{1}{4}\left(\frac{c_1}{c_2}\right)\right]^{-0.5} \quad (12)$$

Pulsed-Field Gradient NMR. Translational diffusion measurements were conducted on a Bruker Avance II spectrometer with a proton ^{1}H resonance frequency of 400 MHz, which was used in conjunction with a Diff60 probe head. All measurements were done at a temperature of 30 ± 1 °C. Due to the reswelling process needed to obtain gels swollen in selective solvent, a homogeneously filled NMR tube could not be realized, which is reflected in a generally poor resolution, where individual proton resonances cannot be distinguished anymore. Therefore, for convenience in sample handling and minimizing convection effects during longer diffusion times, pieces of swollen gel were filled into a standard 4 mm magic-angle spinning (MAS) rotor with a rubber sealing ring. This simultaneously prevents the evaporation of solvent (which for toluene is very relevant). During test measurements of a D_2O/H_2O mixture with a varied diffusion time Δ between 20 and 200 ms, no systematic change in the diffusion coefficient was obtained, suggesting only minimal convection effects and the absence of restrictions due to larger-scale inhomogeneities (such as grain boundaries or bubbles).

For the diffusion experiments, both a simple pulsed-gradient spin–echo (PGSE) sequence and a stimulated-echo sequence with bipolar gradients (PGSTEbp) were applied.[62] Both pulse sequences were used, and the results were recorded for each measured sample. For diffusion of small probes, the difference in molecular mobility (and therefore transverse relaxation time T_2) makes a simple SE an effective sequence for filtering out (or at least reducing) the underlying static contribution of the polymer network. However, as the molecular weight of the probes increases (and the difference in T_2 of gel and probe therefore decreases), the SE sequence imparts a very large T_2-related loss of signal during the increasing diffusion time Δ.

Diffusion coefficients were estimated using the well-known relationship for a Gaussian displacement probability of protons,[63] which is valid for both sequences

$$f(D) = \frac{A}{A_0} = \exp\left[-g^2\gamma^2\delta^2 D\left(\Delta - \frac{\delta}{3}\right)\right] \quad (13)$$

Here, γ is the gyromagnetic ratio of the protons, g is the magnitude of the applied gradient, δ is its pulse length, and Δ is the diffusion time. For discrete distributions of diffusivities (or a nearly nondiffusing background such as a chemically linked polymer network), this approach needs to be modified so that a weighted sum (see equation below) is used for evaluation. If the components are not separated in time scale, a distinction cannot be made properly, and only the inverse average diffusion coefficient D is accessible from the initial slope.

However, as in many cases (except for glucose and PS-1 kDa), we have 1–2 decades between the D's of these components (free diffusion of solvent ~10^{-9} m^2/s vs slow diffusion of probe molecules ~10^{-11} m^2/s vs nondiffusing network ~0), and these components can be distinguished rather clearly in most cases, resulting in a simple relation of two contributions according to eq 13, as well as a constant background signal for the nondiffusing species

$$\frac{I}{I_0} = f(D_{\text{solv}}) + f(D_{\text{probe}}) + \text{cst} \quad (14)$$

Due to the poor resolution originating from the strong field inhomogeneities arising from the gel being packed only as loose pieces within the rotor, unfortunately, there is no possibility of separately integrating peaks belonging to the probe molecule. As there is also no possibility of a sample preparation resulting in a homogeneously filled rotor (note: swelling inside the rotor leads to strong swelling anisotropy that significantly influences the tension of network chains and therefore the mesh size), we numerically separate the diffusion decays of small integrated, spectral windows (of ~0.1 ppm width) into components. A python script was written taking a pseudo-2D data set $\{b, I(\omega_{\text{ppm}}, b)\}$ obtained from the instrument, fitting the slice-based decays $I(b)$ with $b = g^2\gamma^2\delta^2(\Delta - \delta/3)$ in an automated way to eq 14 (see Figure 2). The advantage of this method lies in the identification of regions of integration where a diffusion coefficient for the probe molecules can be identified reliably while also providing an error estimate of this diffusion coefficient by comparing it to values obtained from other slices. By using an additional bar plot of the relative fractions identified by the fit, a picture of the composition of the unidentifiable spectral region can be obtained, further helping in separating the convoluted diffusion decay into distinct components.

In general, the dependence of the long-range diffusion coefficient of polymer molecules D on the molecular weight M is well-known, both by theory and experiments,[64] and it can be described by a power law model, where α is the scaling exponent that may change depending on solvent quality, polymer concentration, and overall polymer conformation

$$D = \frac{k_B T}{6\pi\eta R_h} \propto M^{-\alpha} \quad (15)$$

https://doi.org/10.1021/acs.macromol.3c02139
Macromolecules XXXX, XXX, XXX–XXX

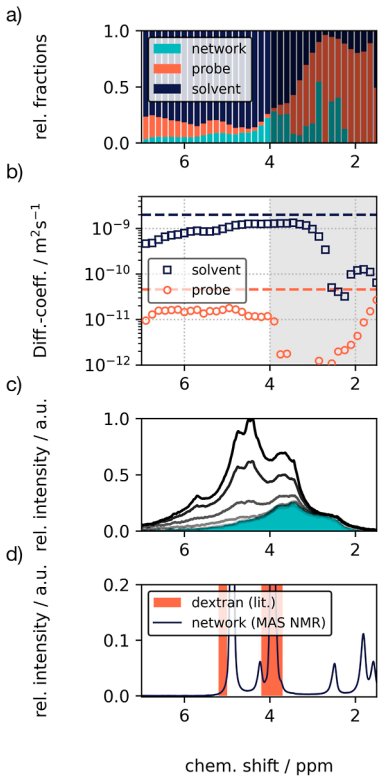

Figure 2. Exemplary analysis results of the PGSE experiment for dextran-20 kDa within the PEG−PCL network as described in the text. (a) Fractions shown as bar plot for each slice (Δ_{ppm} = 0.15 ppm) within the ppm region according to eq 14. The shaded area corresponds to the region where the automated fit procedure is unstable. (b) Diffusion coefficient of both fast (solvent) and slow (probe) components corresponding to each slice, with the shaded region revealing the fitting instabilities. (c) T_2-filtered (Δ = 25 ms) proton ^{1}H NMR spectrum for different gradient strengths. The constant background arising from the remaining network after the T_2-filter is shaded in blue. (d) Exemplary ^{1}H-MAS NMR spectrum of our ACNs in D_2O, as well as theoretical peak positions of dextran (red rectangles). The fitting instabilities are due to the strong network contribution, leading to an inadequate attribution of the network component to the dextran fraction. The strong overlap of network and PSC resonances around 3.6−4 ppm restricts integration to the broadened −OH resonance at around 5 ppm.

For a random-coil polymer in a good solvent diffusing without restriction (in the nondraining Zimm limit), an exponent between 0.5 and 0.6 is expected and experimentally confirmed, e.g., in ref 65. In the past, diffusion data of macromolecules through the mesh of chains in swollen networks have often been analyzed via empirical relations holding for globular/colloidal probes, such as $D/D_0 = \exp(-R_h/\xi)$, where ξ was assumed to be the mesh size.[19,66] Here, we follow a more polymer-physical rationale, based upon the insight that diffusion of macromolecules through a network resembles the diffusion through a semidilute polymer solution,[67] requiring the discussion of the appropriate scaling regimes. Given the probe self-diffusion in good solvent is in the Zimm limit (α = 0.588), we thus expect a crossover into the Rouse regime with dominating single-segment friction (α = 1, "free-draining limit") or even stronger scaling once entanglements become important, e.g., α = 2 for the simple reptation model.[68] The first of these transitions to α = 1 is expected when the probe size becomes comparable to the hydrodynamic screening length ξ_h; the second transition is expected for molecules of a size comparable to the diameter of an entanglement tube. There is experimental evidence[51] that ξ_h in a semidilute solution or a polymer network is close to the static correlation length ξ_c.[64]

$$\xi_h \approx \xi_c \approx b\left(\frac{b^3}{\nu}\right)^{(2\nu-1)/(3\nu-1)} \phi^{-\nu/(3\nu-1)}$$

Here, b is the root-mean-square size of a Kuhn segment, ν the excluded volume parameter of a Kuhn segment, and ϕ the volume fraction of polymer inside the gel. In what follows, we adopt the approximation $\xi_h = \xi$ for discussing the dilute and semidilute unentangled regime of swollen or ideal probe chains inside a gel. A linear chain made of N Kuhn segments and with a size $R < \xi$ develops Zimm dynamics similar to a dilute solution with a diffusion coefficient following eq 15 with $R_h = bN^\nu$ and $\alpha = \nu$.[31,64] For chains with a size $R > \xi$, i.e., for polymer volume fractions beyond the overlap polymer volume fraction[69]

$$\varphi^* \approx \frac{Nb^3}{R^3}$$

the dynamics follows the Zimm model up to the correlation length ξ with a friction coefficient[64]

$$\zeta \approx \eta_s \xi$$

at the correlation length ξ. On length scales exceeding ξ, these dynamics are followed by Rouse dynamics, where correlation volumes with[64]

$$g \approx \left(\frac{b^3}{\nu}\right)^{3(2\nu-1)/3\nu-1} \varphi^{-1/(3\nu-1)}$$

Kuhn segments establish N/g effective Rouse monomers resulting in a diffusion coefficient of

$$D \approx \frac{kT}{\zeta}\frac{g}{N} \propto \left(\frac{b^3}{\nu}\right)^{2(2\nu-1)/3\nu-1} \varphi^{-1-\nu/3\nu-1} N^{-1} \quad (16)$$

In a comparison between the diffusion coefficients D of the probe polymers inside the gel at a polymer fraction ϕ and correlation length ξ_c and the diffusion coefficients D_0 measured in a polymer solution (as described above) at $\phi_0 \approx 1/20$ and correlation length ξ_0, we expect a crossover from $D/D_0 = 1$ for small probe polymers of size $R < \xi_0$, ξ toward the Rouse limit ($R > \xi_c$, ξ) with the following asymptotic ratio

$$\frac{D}{D_0} \approx \frac{g_0\xi}{\xi_0 g} \approx \left(\frac{\varphi}{\varphi_0}\right)^{-(1-\nu/3\nu-1)} \quad (17)$$

A crossover between both limits occurs for $\xi < R < \xi_0$. According to the above equations, this crossover is described by

$$\frac{D}{D_0} \approx \frac{gbN^\nu}{\xi N} \approx \left(\frac{b^3}{\nu}\right)^{2(2\nu-1)/3\nu-1} \left(\frac{\phi}{\phi^*}\right)^{-(1-\nu/3\nu-1)} N^{-(1-\nu)} \quad (18)$$

The crossover between the low-R regime and the transition zone allows for a rough estimate of ξ_h by extrapolation of the reduced diffusion coefficient in the crossover region toward $D/D_0 = 1$, yielding the relevant length scale $\xi_h \sim R$ governing the diffusion process.

Viscosimetry. The viscosity of 5 wt % solutions of PSCs and PSs with different sizes was measured using a RheoSense m-Vroc equipped with a 20 μL sample cell and a 500 μL Hamilton syringe. All solutions were measured at 5 wt % concentration at T = 30 ± 0.2 °C using 4 different flow rates between 100 and 800 μL/min and two measurements per flow rate for each sample. The final value was determined using the average of the 8 viscosity values obtained. In case the standard deviation of the mean remains below the error given by the manufacturer (2.5%), the latter number is used.

Magic-Angle Spinning Double-Quantum NMR. Double-quantum (DQ) MAS NMR experiments were carried out on a Bruker Avance III 400 MHz spectrometer with a 4 mm triple-resonance MAS probe

https://doi.org/10.1021/acs.macromol.3c02139
Macromolecules XXXX, XXX, XXX−XXX

at a spinning frequency of ν_{rot} = 5 ± 0.01 kHz. A small, round 4 mm × 0.2 mm slice of a swollen polymer network is packed tightly into a rotor, being surrounded by tightly fitting PTFE cylinders in order to stabilize the rotor. A Bruker BVT 3000 was used to keep the temperature stable at T = 30 ± 1 °C. As a chemical shift reference, values obtained in ref 49 were used. POST-C7 experiments[70] were conducted using pulse lengths (power) of $p90$ = 2.5...3 μs (39 W) and $p7$ = 3 μs (6.8 W), such that the necessary condition of $\omega_{nut} = 7\nu_{rot}$ is fulfilled. Using this sequence, a recoupling of the homonuclear ^{1}H−^{1}H interactions is performed, and DQ coherences are excited and detected after reconversion and DQ filtering via a phase cycle. Thereby, the motion-averaged residual dipolar coupling D_{res} can be accessed while maintaining resolution along the chemical shift axis, which allows for qualitative information about the orientational degree of freedom of the PEG and PCL moieties, respectively (see Figure 9).

As already discussed elsewhere in the context of polymer networks, e.g., in refs 49 and 71, the experiment yields a set of two signal functions depending on the DQ pulse sequence duration (τ_{DQ}), which together can be used to estimate D_{res}. One can either calculate the normalized relaxation-free DQ buildup curve $I_{nDQ}(\tau_{DQ})$ or use a simultaneous fitting procedure in the references above. Due to experimental observations that will be explained later on, the former approach was chosen using the well-established equation for the DQ build-up curve (the Abragam-like function) of a single D_{res}[72]

$$I_{nDQ}(\tau_{DQ}) = 0.5[1 - \exp(-(0.378\epsilon D_{res}\tau_{DQ}))^{1.5} \cdot\cos(0.583\epsilon D_{res}\tau_{DQ})] \quad (19)$$

Here, ϵ = 0.232 denotes the scaling factor for this pulse sequence. As the gels studied are rather soft and the centrifugal forces due to spinning are not negligible, the D_{res} values obtained will be subject to potentially strong bias and therefore reflect the elastic response of the network chains[73] only qualitatively. However, comparisons between PEG and PCL network chains based on relative differences in D_{res} can still be made, despite the possibility of minor narrowing effects in the range of observed D_{res} values due to differences in the elastic response of these moieties.

RESULTS AND DISCUSSION

Structural Aspects from SAXS Experiments. *Swelling in Common Good Solvent.* Exemplary scattering data are shown in Figure 3. Networks in good solvent were fitted (see the Appendix for plots) with the approach described in the SAXS subsection using eq 2. While the large-scale fluctuations are not accessible from SAXS in a meaningful way, they still have a significant contribution requiring at least a placeholder function for ensuring a proper fit. In most cases, the Ornstein−Zernike function, characterizing the liquid-like fluctuations with correlation length ξ_c, is clearly visible, and it can easily be deconvoluted from the data obtained. Only for the PEG−PEG network at $c = 0.7c^*$, the distinction between the Ornstein−Zernike function and the Debye−Bueche placeholder function is getting rather ambiguous. Nevertheless, the results plotted as a function of preparation concentration (see Figure 4) show data with low random scatter that can be fitted using a simple power-law model $\xi(\phi) = a\cdot\phi^{-\beta}$ as expected.[69] While both sample series of PEG−PCL and PEG−PEG ACNs show a similar scaling behavior, respectively, of $\beta = -0.83 \pm 0.2$ and $\beta = -1.08 \pm 0.05$, we notice a deviation of β from the literature value ($\beta = -0.75$ for a semidilute solution of chains in good solvent). This discrepancy will be discussed in detail in a future publication.

At the overlap concentration c^* (here: $\phi^* = 0.06$), we estimate ξ_c of our networks in good solvent to be $\xi_c = 4.9 \pm 0.2$ nm (uncertainty from fit) for the PEG−PCL networks and $\xi_c \approx 4.7 \pm 2.0$ nm (uncertainty by systematic variation of β) as an extrapolated value for the PEG−PEG networks at $c = c^*$. Finally, it is found that both types of networks with the same coupling chemistry also result in approximately the same correlation length over a range of concentrations from 0.7−3c^*, indicating that no severe mixing issues were encountered during the synthesis of the amphiphilic PEG−PCL system. For the well-known tetra-PEG−water system (θ solvent) described by Sakai et al. for a star size of 10 kDa, a value of $\xi_c \approx 2.2$ nm can be interpolated from data reported in ref 74 at $c = c^*$. While not directly comparable, this serves as a rough guide concerning the order of magnitude.

After the drying process, open chain ends may undergo a postcuring reaction in bulk due to their spatial proximity at an increased effective overlap number, resulting in cross-linked networks strands that, upon swelling, will be highly stretched (see ref 49 for additional data on the impact on the equilibrium swelling degree). Thus, we conducted experiments on PEG−PCL networks, subjecting them to a drying process in a vacuum oven followed by reswelling to values close to their degree of swelling at preparation (mimicking the preparation procedure utilized in diffusion experiments). As seen in Figure 4, the correlation length decreases strongly by a factor of about 4−5 at c^* and about a factor of 2 at 3c^*, resulting in a change

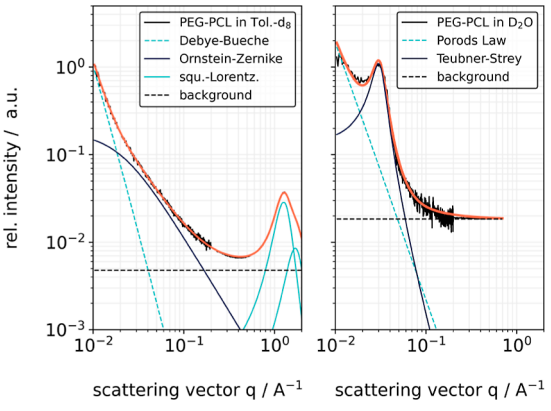

Figure 3. Exemplary scattering curves, as well as their respective evaluation, for the investigated PEG−PCL ACN in nonselective solvent (left) and selective solvent (right).

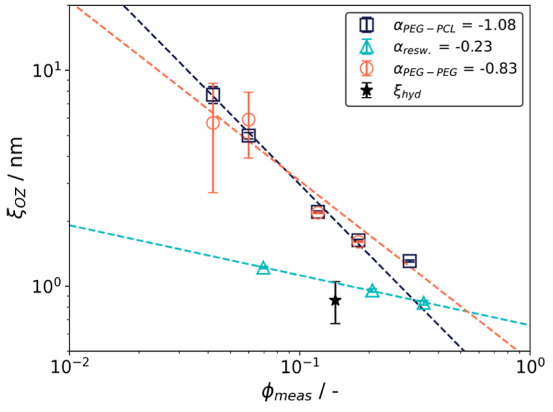

Figure 4. Correlation length ξ obtained from the evaluation of different networks measured in good solvent and as-prepared (or reswollen to preparation condition) in dependence of the preparation condition and fits with power laws ϕ^{α}.

https://doi.org/10.1021/acs.macromol.3c02139
Macromolecules XXXX, XXX, XXX−XXX

of the slope to $\nu = -0.23$. In a preceding work, we recognized a large change in the equilibrium degree of swelling after drying the samples.[49] This was explained by a postcuring process in the dry state leading to two classes of chains cross-linked at different polymer volume fractions. This scenario implies that the chains linked in the dry state will be largely stretched at swelling equilibrium. The scattering intensity is the superposition of the scattering intensity of the tension blobs of these stretched chains with the correlation volumes of all other chains. We speculate that this superposition impacts the analysis of the correlation length of samples that were swollen after drying. As our data quality does not allow for an estimation of the exponent ν needed in eq 3, we continue to use $\nu = 0.588$, even though the stretched chains are supposed to have a higher exponent. This is again taken up in a future publication.

Swelling in Selective Solvent. The SAXS measurements on the phase-separated networks swollen in poor solvent for PCL (D_2O) were analyzed (see Figure 3 for an exemplary comparison in both solvents and Figure 5 for length scales extracted) using eq 5 in conjunction with the TS model for MPS in emulsions (eq 10), as well as a comparative evaluation using the hard-sphere model of KT; see Appendix for a comparison of plots. The evaluation of the data sets using the TS model yields two length scales reflecting the distance d_{TS} between the scattering moieties (see eq 11), as well as an associated decay length ξ_{TS} (see eq 12). The former is interpreted as an average center-to-center distance between the clusters, while the latter gives a length scale of a still constructive interference of radial oscillations of individual $g(r)$, which later on will be compared to the estimated cluster size. However, it should be stressed again that these length scales are defined in terms of correlation functions, rendering these mappings only qualitative. While the Ornstein−Zernike function for the modeling of the network correlation length is still needed to model the experimental data, a constant correlation length ξ_c is not expected due to the spherical domains covered by a spherical grafted layer of PEG chains with an increasing blob size as a function of the distance to the PCL domains. Across a wide range of preparation concentrations (and associated network chain connectivity distributions, see ref 49), we find nearly constant values for both average distance and decay length of the microphase-separated domains, being $d_{TS} \approx 18.5$ nm and $\xi_{TS} \approx 7.8$ nm, respectively.

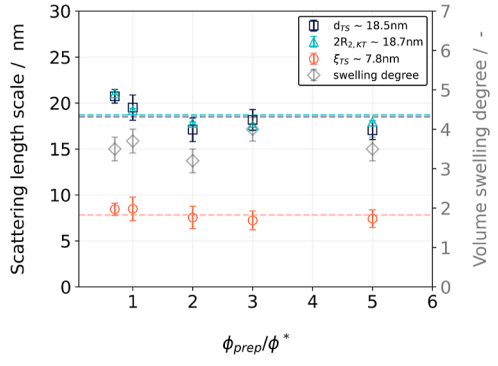

Figure 5. Overview over the length scales obtained (domain distances d_{TS}, as well as domain-associated correlation length scale ξ_{TS}) from eqs 11 and 7 for the model according to TS and KT, respectively.

In a simple model of spheres of bulk-like PCL interconnected by chains of PEG, the core−core distance should at maximum be equal to the length of a stretched PEG chain plus a collapsed PCL chain (with the collapsed PCL being localized within the spanned sphere), which will be enough to satisfy the spatial requirements of both models to be analyzed in the following (see Appendix for all chain length scales used in the following). An estimate of the cluster radius $r_{cluster}$ can be obtained using a combination of the distance between the clusters d_{TS} and the swelling degree Q (see Figure 5), which is approximated as $Q \approx 4$ (resulting in selective swelling degrees of $Q_{PEG} = 7$ and $Q_{PCL} = 1$) for simplicity. Using either a simple cubic (sc) lattice distribution of close-packed clusters or a close-packing of spheres [face-centered cubic (fcc)], we arrive at packing densities of $s_{sc} = 0.5236$ and $s_{fcc} = 0.7406$, respectively, both of which are too large for the volume taken up by the PCL spheres having $s_Q = 0.125$ as calculated from the swelling degree. Therefore, it can be immediately concluded that $d_{TS} > 2r_{cluster}$ (no direct contact between the spheres) with the relation between d_{TS} and $r_{cluster}$ being described by the experimental volume occupancy s_Q and the assumed spatial geometry. The effective shrinkage factors of the spheres (needed to realize this morphology) are thus calculated as $k_{sc} = (0.125/0.5236)^{1/3}$ and $k_{fcc} = (0.125/0.7406)^{1/3}$. With that, we arrive at

$$r_{cluster,sc} = 0.31 d_{TS} = 5.73 \text{ nm}$$

$$r_{cluster,fcc} = 0.28 d_{TS} = 5.18 \text{ nm}$$

for the respective geometries. As the cluster radius obtained is significantly different from the decay length $\xi_{TS} = 7.8$ nm of the TS model, it emphasizes the fact that ξ_{TS} cannot be used as an estimate for the cluster radius. With $r_{cluster}$ calculated, we can estimate the aggregation number (number of stars participating in a cluster) as

$$\text{AN} = \frac{\frac{4}{3}\pi r_{cluster}^3}{M_{star}/(\rho_{star} \cdot N_A)} \approx \frac{r_{cluster}\ [\text{nm}]^3}{3.81\ \text{nm}^3} \quad (20)$$

Here, $M_{star} \approx 11\,000$ g mol^{-1} is the molecular weight of the PCL star and $\rho_{star} = 1.145$ g cm^{-3} is the density of PCL. The respective aggregation numbers can be calculated as $AN_{sc} = 49$ and $AN_{fcc} = 36$, respectively. Therefore, from the TS model alone, no reliable estimate concerning the aggregation number can be made due to the fact that calculations using the swelling degree rely on a priori assumptions of the spatial cluster arrangement. Nevertheless, as will be discussed later on, the cluster radii calculated are in good agreement with a bond-fluctuation model (BFM) simulation on the given system, while the aggregation numbers show deviations arising mainly from geometric assumptions as well as small uncertainties in $r_{cluster}$ that are getting amplified by the scaling of AN $\propto r_{cluster}^3$.

An alternative evaluation using the KT model (see Appendix for the fits) assumes a hard-sphere form factor with a radius of R_1 for the microphase-separated domains (possibly biased by contrast from a higher-concentrated PEG phase surrounding it), along with an outer "soft" yet entropically strongly repulsive corona of radius R_2 that does not contribute to the scattering contrast, but provides the link to the assumed PY hard-sphere structure factor. For all curves, a somewhat

https://doi.org/10.1021/acs.macromol.3c02139
Macromolecules XXXX, XXX, XXX−XXX

artificial behavior concerning the obtained radii is found: the values of R_1 and R_2 converged toward each other for all concentrations, resulting in $R_1 \approx R_2 \approx 9$ nm and a volume fraction of the R_2-spheres ranging from $\eta = 0.14-0.17$ for all samples (being reasonably close to the PCL volume fraction of 0.125 as governed by the PCL content and the swelling degree). The logarithmic standard deviation was around $\sigma = 0.3-0.4$ for all measurements, indicating distributions being less than half a decade wide. As η constitutes the volume fraction of the clusters including the repulsive corona, a contradiction to the observed swelling degree of $Q \approx 4$ (leading to $\eta \approx 0.125$) arises. While the radii obtained from the KT model appear to be overestimated, the volume fraction indicates a diluted system of clusters. Thus, we refrain from an interpretation of R_1 as $R_{cluster}$ and calculation of d_{KT}.

Reasons for the inconsistent trends of the KT-model fitting parameters may include the difficulty to assign correct length scales due to a possibly significant change in scattering contrast between the water-swollen PEG phase and the more concentrated PEG corona, rather than between the collapsed PCL and PEG domains. Alternatively, the spatial arrangement of the clusters may be at least partially affected by the topological constraints of the network and not fulfill the assumption of the Percus−Yevick structure factor of an equally probable arrangement of clusters once a critical distance qR^* has been surpassed. Finally, the constraints may affect the shape of these clusters, deviating from the perfectly spherical shape as, e.g., found in micellar systems, but rather be distorted and anisotropic.

However, as the values of $R_{1,2}$ nearly perfectly match the results from the TS model (see Figure 5), once $2R_2 \approx d_{TS}$ is assumed, we just notice that this results in a probably overestimated aggregation number of AN = 53, matching the sc lattice interpretation of the TS fits. We should finally stress that fitting of the rather featureless scattering data with more elaborate models, possibly accounting for contrast variations inside the swollen phase or structural details, entails a significant risk of overinterpretation and even more serious systematic uncertainties.

As a last step, our assumptions thus are compared to lattice-based BFM Monte Carlo simulations on a model system designed to match the synthesized PEG−PCL conetworks in terms of chain dimensions and thermodynamic conditions, see Figure 6 and selected data in Table 1.

The parameters of the BFM model were chosen in accord with known segment sizes of PEG and PCL, giving a lattice unit of approximately $u = 0.33$ nm and an average bond length of 0.87 nm. The simulation volume consists of a cube of $L = 256u = 84$ nm, and the phase-separated system in a selective solvent shown in Figure 6 assumes a smaller spherical volume with a diameter in the same range. Further details on the simulation model can be found in ref 50, where we have discussed the swelling in a nonselective solvent simulated implicitly as empty lattice sites. For selective swelling, we moved to an explicit solvent with tunable interaction energies, where PCL collapse is induced by changing the PCL−solvent interaction energy. The detailed results and analyses of these simulations studies (including the simulation of scattering data) are beyond the scope of the present contribution and will be published separately. Therefore, simulation results shown in this work are only of qualitative nature, and selected data is shown for the purpose of showcasing the good agreement of

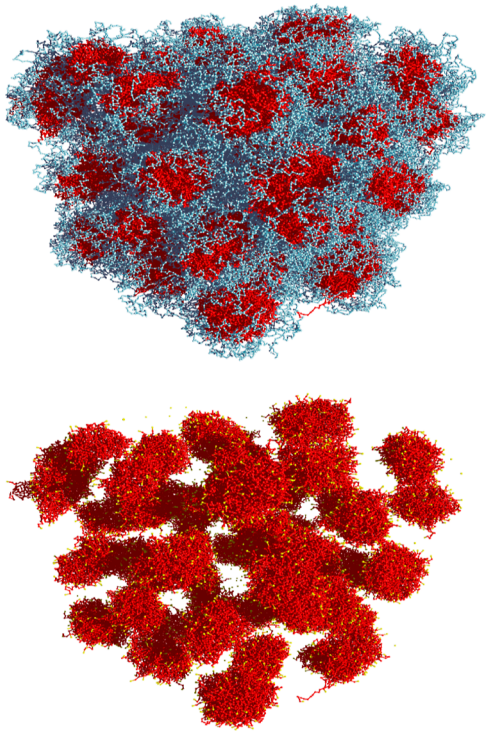

Figure 6. Snapshot of the simulated microphase-separated PEG−PCL system in a poor solvent investigated using BFM simulations for $\phi = 3\phi^*$. Top: all simulated monomers (PEG chains in light blue, PCL chains in red). Bottom: same data, but with the PEG chains being invisible, thus revealing the ellipsoidal shape of the PCL domains. The cross-linking groups (outermost monomer of the PEG star branches) are colored in yellow, revealing that they primarily reside at the outer shell of the PCL cluster. The simulated polymer slab can be mapped on a size of about 84 nm, so individual PCL clusters have a diameter of around 14 nm with substantial anisotropies, as reported in Table 1.

Table 1. Selected Real-Space Simulation Results for Different Preparation Concentrations ϕ_0 Normalized by ϕ^*[a]

ϕ_0/ϕ^*	$\langle N\rangle$	$Đ$	R_g (nm)	$l_x/l_y/l_z$
1	17.39	1.15	4.69	1.42:1.17:1
2	20.52	1.16	5.16	1.66:1.20:1
3	24.49	1.17	5.70	1.86:1.24:1
4	24.70	1.26	6.32	2.02:1.22:1

[a] $\langle N\rangle$: average number of stars in the clusters; $Đ$: distribution width (polydispersity) given by $\langle N^2\rangle/\langle N\rangle^2$; R_g: cluster radius of gyration; l_{xyz}: relative axis length after projection onto an ellipsoid, quantifying the cluster anisotropy. In the limit of a massive sphere, the geometric radius R is larger than R_g by a factor of $(5/2)^{1/2}$, compare caption of Figure 6 for $\phi_0 = 3\phi^*$.

experiment and simulation and providing an additional anchor for the interpretation of the scattering data.

Here, we just discuss preliminary data on the simulated real-space MPS structure, which most importantly reveals that the clusters are not in direct contact with each other and consist of about 17−25 stars per cluster with a narrow size distribution corresponding to a polydispersity of about 1.1−1.2 (see Table 1). It should be noted that the simulation needs to assume a PCL−water interaction parameter which was not yet identified (or mentioned in literature). As the cluster size depends on this parameter, the hereby presented values only constitute an estimate. The simulations confirm the assumption that the

https://doi.org/10.1021/acs.macromol.3c02139
Macromolecules XXXX, XXX, XXX−XXX

clusters are nearly free of PEG chains and further reveal an ellipsoidal/worm-like shape (which may thus impart a systematic error on fitting results). The simulations further show a slight dependence of the structural parameters on the initial preparation concentration, whereas this is not found in our measurement. A possible explanation for this difference is that the drying and reswelling process of the experiments may erase these concentration dependencies. Alternatively, these dependencies could also be an artifact of the finite number of star polymers growing with concentration in the simulations since the largest domains surrounded by the densest polymer coronas are found toward the middle of the simulation box.

Diffusivity in Solutions of Probe Molecules. As a first step, the diffusivity of the PSC and PS probe molecules was studied in solution without the presence of the polymer network in their respective solvents using the PGSTEbp sequence. By plotting the logarithmic inverse diffusion coefficient over the logarithmic molecular weight (see Figure 7), a linearization of eq 15 is performed. For the PSCs, the shape reveals a scaling exponent of $\alpha = 0.58 \pm 0.03$ (slightly elevated in comparison to that in ref 66), while for the PS probes, a similar exponent of $\alpha = 0.63 \pm 0.04$ is found (in agreement with those in other works[75,76]). In both cases, the exponents match the expected values from theoretical models for self-diffusion in the good solvent and dilute solution.[69] The concentration dependence of the diffusion coefficient of PSCs in water was not validated again in our study as this was already examined by Wallace *et al.*[66] for a 2000 kDa dextran up to 3 mg mL^{-1}. Overlap concentrations of 80− 120 g L^{-1} are reported for a 2000 kDa dextran elsewhere,[77,78] which is higher than the concentration and molecular weight used in our study. Therefore, intermolecular interactions will be disregarded in the following discussions. For both types of probe molecules, the viscosity of the respective solutions η was measured at similar concentrations and used for estimating the hydrodynamic radius R_h according to the Stokes−Einstein relation, eq 15.

For the PSCs, these results are compared to Braeckmans' empirical relation,[79] which relates R_h and M_w of a given dextran

$$R_h\ [\mathrm{nm}] = 0.015(M_w\ [\mathrm{kg\ mol^{-1}}])^{0.53\pm0.02} \tag{21}$$

As seen in Figure 7, the hydrodynamic radii as calculated from the measurements of diffusion coefficient and viscosity (eq 15) are consistently somewhat smaller than the theoretical prediction according to eq 21, which was also found by Wallace et al.[66] The latter work attributes this to the presence of a significant portion of PSCs with lower molecular weight than given, which is also based on the exponent of eq 15 being significantly lower than that expected due to an increasing difference in theoretical and measured hydrodynamic radius with increasing molecular weight. In contrast to that, we retain the expected exponent of eq 15 ($\alpha = 0.58 \pm 0.03$) while also finding no curvature in the observed PGSTEbp diffusion decays, suggesting that the PSCs used consist of a smaller size or alternatively contain, e.g., a significant number of branches that reduce the effective hydrodynamic radius.

For the solutions of PS in toluene, Fetters et al.[80] summarized existing literature on the hydrodynamic properties of the PS−toluene system and eventually arrived at the following equation yielding a nearly perfect regression model across different methods applied to dilute solutions

$$R_h\ [\mathrm{nm}] = 0.0108(M_w\ [\mathrm{kg\ mol^{-1}}])^{0.569} \tag{22}$$

Unfortunately, usage of eq 22 indicates that our solutions of 5 wt % PS are already too close to the overlap concentration, challenging viscosity at the zero-concentration limit as required for eq 15, see Figure 7, bottom right. A significant deviation occurs for the 70 and 100 kDa samples, which can be explained by polymer−polymer interactions and chain interpenetration effects arising from incipient coil−coil overlap (e.g., ref 81 finds an overlap concentration of a 48.8 kDa linear PS at $c \approx 4.5$ wt %). Hence, we will resort to literature values obtained from eq 22, as our current setup. Moreover, the evidence of a semidilute solution of PS polymers in our observation underlines the motivation for using models that necessitate probe molecules to be in the Zimm limit.

Hydrodynamic Screening Length from Probe Diffusion. Diffusivities of both types of probe molecules are measured within the polymer network (see Table 2) using the procedure described in the Methods section for an identification of the PSC diffusion coefficients, while for the PS probes, a simple integration of the styrene proton resonances at 6−7 ppm was possible and sufficient. In both cases, a log−log plot (Figure 8) of the reduced diffusion coefficients D/D_0 vs M_w shows a power-law behavior that can be evaluated by the model for polymer dynamics described before. For probe molecules of small size, we expect diffusion coefficients D comparable to the free diffusion coefficients D_0 up to minor deviations. Once the size of the chain R (or the corresponding molecular weight M_w) becomes comparable to the hydrodynamic screening length of the gel ξ_h, we expect a transition from the nondraining Zimm limit toward the crossover regime and Rouse limit. As seen by examination of

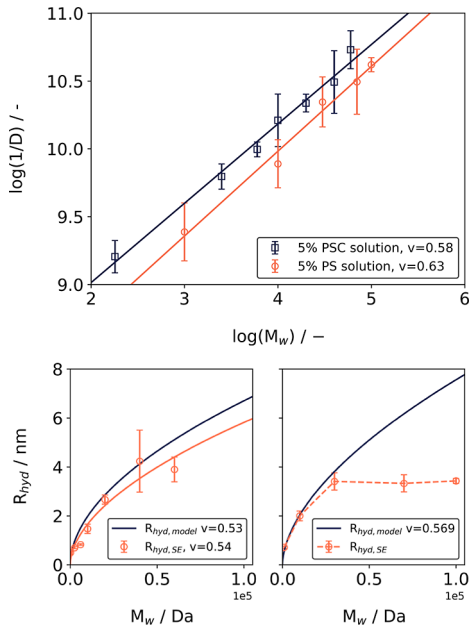

Figure 7. Top: log−log-plot of the inverse diffusion coefficient D in m^2/s vs the molecular weight M_w in 5 wt % solutions of PSCs and PSs. Fits were carried out according to eq 15, leading to exponents of $\alpha = 0.58 \pm 0.03$ and $\alpha = 0.63 \pm 0.04$ for the PSCs in D_2O and PSs in toluene-d_8, respectively. Bottom: hydrodynamic radius R_{hyd} of the PSCs (left) and PSs (right) is plotted against M_w for both the estimated values according to eqs 21 and 22 and estimated values from measurements of diffusivity and viscosity using eq 15.

https://doi.org/10.1021/acs.macromol.3c02139
Macromolecules XXXX, XXX, XXX−XXX

Table 2. Free-Probe Diffusion Coefficients (D_0) in Solution and the Corresponding Reduced Diffusion Coefficients in the Networks (D/D_0) for the Different Probes at T = 30 °C

PSC			PS		
M_w (kDa)	D_0 (10^{-10} m^2/s)	D/D_0	M_w (kDa)	D_0 (10^{-10} m^2/s)	D/D_0
0.18	6.04 ± 0.74	1.10 ± 0.18	1.0	4.09 ± 0.87	0.78 ± 0.24
2.5	2.66 ± 0.15	0.64 ± 0.17	10.0	1.29 ± 0.23	0.41 ± 0.07
6.0	1.87 ± 0.06	0.73 ± 0.09	30.0	0.45 ± 0.08	0.27 ± 0.06
10.0	0.94 ± 0.12	0.42 ± 0.22	70.0	0.32 ± 0.08	0.13 ± 0.04
20.0	0.46 ± 0.03	0.37 ± 0.16	100.0	0.24 ± 0.01	0.11 ± 0.02
40.0	0.25 ± 0.07	0.29 ± 0.09			
60.0	0.21 ± 0.03	0.24 ± 0.11			

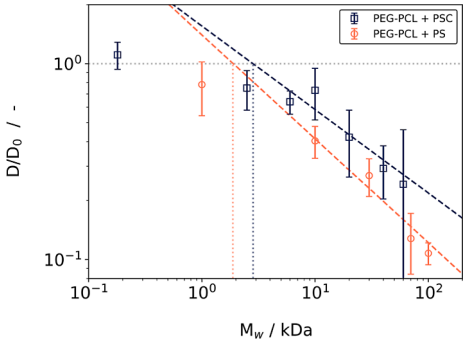

Figure 8. Reduced probe diffusion coefficients plotted against the respective M_w. In the Zimm limit, we expect $D/D_0 \approx 1$ for small M_w, whereas a transition according to the scaling of eq 18 is expected upon increasing M_w. The extrapolation of the latter regime toward D/D_0 yields M_w = 1.88 ± 0.8 kDa for the PS probes and M_w = 2.83 ± 1.5 kDa for the PSC probes, resulting in hydrodynamic radii of R_h = 0.78 ± 0.19 nm (PS in toluene-d_8) and R_h = 0.83 ± 0.23 nm (PSC in D_2O).

the slope of the data in the figure, we do not access the final Rouse limit but only the crossover regime described by eq 18.

For both types of probe molecules, the exponent of the data with M_w > 3 kDa in Figure 8 is close to −1/2 (α_{PS} = −0.53 ± 0.08 and α_{PSC} = −0.42 ± 0.13) with a significant error, such that the expected exponents of −0.42 for a good solvent and of −0.5 for a θ solvent are not entirely out of reach. The hydrodynamic screening length $\xi_h \approx R_h$ is obtained by extrapolating the crossover regime toward D/D_0 = 1. From the extrapolation, we obtain M_w = 2.83 ± 1.5 kDa (equivalent to R_h = 0.83 ± 0.23 nm according to the interpolation of the measured R_h above) for the network swollen in water (nonsolvent for PCL), as well as M_w = 1.88 ± 0.8 kDa (R_h = 0.78 ± 0.19 nm according to eq 22) for the network swollen in toluene-d_8 (good solvent for the whole ACN). For the PS probes, we may alternatively resort to a calculation of R_g assuming a linear chain and using a Kuhn length of 1.8 nm[64] and a Kuhn molar mass of 720 g mol^{-1},[64] resulting in R_g = 1.3 nm. Now, we can obtain R_h using the relation of $R_g = r \cdot R_h$ with r = 1.5 for a linear chain in a good solvent[17] for the conversion, resulting in R_h = 0.86 nm, which lies within the error margin provided above. Therefore, it is found that no significant difference between the diffusion of probe molecules in their respective good solvents is found for both types of network architecture, indicating that the PCL clusters act as localized obstacles that do not significantly influence the diffusion of probes in between. Small differences arising from an accidental mismatch of the swelling degrees (as the selective swelling of the PEG phase in D_2O will result in $Q \approx 7$, whereas $Q \approx 5$ in toluene-d_8) can be approximated by an expected scaling of the end-to-end distances and result in a factor of $c = (7/5)^{1/3}$ = 1.11, which in turn would result in ξ_h = 0.70 ± 0.17 nm for the PS in toluene-d_8 at a hypothetical swelling degree of Q = 5 and ξ_h = 0.83 ± 0.23 nm for the PSC in D_2O at the same swelling degree (which is still within the provided error bars).

It should be noted that the values obtained are valid only for the samples exposed to the drying−reswelling process, which is needed for cleaning the sample from sol. Hence, we assume that the aforementioned overlap with highly stretched chain conformations will also dominate the values for ξ_h obtained hereby. Consequently, our value obtained in good solvent (ξ_h = 0.78 ± 0.19 nm) is to be compared with the interpolated correlation length at an equivalent polymer volume fraction of $\phi \approx 1/6$ being ξ_c = 1.01 ± 0.06 nm (see Figure A1 for ξ_c after the drying + reswelling process), yielding an acceptable agreement, acknowledging that ξ_h and ξ_c are roughly equal, although being estimated via two independent methods.

Concerning the estimation of length scales governing the diffusion process, we note that a significant amount of literature commonly uses colloidal models such as an obstruction-based model or the hydrodynamic model of Cukier,[18] both assuming the existence of a well-defined polymer mesh with a defined *mesh size* of length scale ξ_{mesh}, as well as a *rigid colloidal probe*. For linear PS chains, the latter assumption is clearly not fulfilled, whereas for the PSCs, there exists at least experimental evidence that these tend to form branched structures that may justify such behavior up to $R_h \leq \xi_{mesh}$. Based on Figure 8, we may use at maximum the first 3−4 points for an exponential fit to a simple obstruction model of the form $D/D_0 = \exp(-R_h/\xi_{mesh})$, which yields a rather undefined and probably underestimated value for the geometrical mesh size as seen by a PSC probe of ξ_{mesh} = 2.4 nm (data not shown), which is significantly smaller than the result of a rough chain size calculation (≈6 nm). This, again, strengthens our motivation to estimate the length scale governing the diffusion process of the given probe molecules only in terms of polymer scaling laws instead of trying to estimate the geometrical mesh size using arguably unjustified hydrodynamic model assumptions.

Anisotropy of Local Segmental Motion Studied by MAS DQ-NMR. As already outlined before, MAS DQ-NMR allows for a qualitative statement on the motional restrictions imposed upon certain parts of the polymer network by its neighboring cross-links or structural features such as MPS by analysis of RDCs reflecting segmental dynamic order parameters of chemically distinct moieties. Using proton spectra assignments of our PEG−PCL ACNs from ref 49 we define the following three regions of interest for our analysis (see Figure 9): the backbone region of the PEG and PCL

https://doi.org/10.1021/acs.macromol.3c02139
Macromolecules XXXX, XXX, XXX−XXX

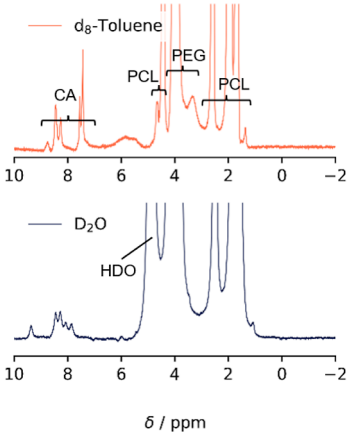

Figure 9. ^{1}H MAS NMR spectra of the ACN (both prepared at $c = c^*$) at $\nu = 5$ kHz spinning. Top: spectrum at preparation conditions in toluene-d_8; bottom: spectrum after drying and reswelling in D_2O at $Q_{eq} \approx 4$. The brackets indicate the integration regions for the DQ build-up curve analysis in Figure 10 (overlap with solvent peaks poses no problem due to the isotropic tumbling, separating it upon analysis).

chains as well as a unique proton peak arising from the oxazinone-based coupling agent [in short: coupling agent (CA) region]. Two networks were synthesized at $c = c^*$, and one of them was measured in toluene-d_8 at the preparation condition, whereas the other network was dried and swollen to equilibrium in water ($Q_{swell} \approx 4$). Despite the multimodal DQ build-up found in our earlier publication,[49] applying low-field NMR measurements, in this work, we observe rather unimodal, albeit distorted, build-up functions for both solvents (see Figure 10), and therefore, we can assign a single representative RDC value to each region. The reason for this unimodality is supposed to arise from the strong rotational forces of from the MAS rotor spinning, which leads to an inhomogeneous stretching of the sample perpendicular to the axis of rotation or alternatively the interface orientation effect of the coupling agent, which will be explained in the following paragraphs.

By comparing the RDC values of the good- and poor-solvent case (see Table 3), we find a strong increase in the RDC value of the linker region (factor $f_{CA} \approx 10$), whereas, surprisingly, both the PEG and the PCL region only show increases of about $f_{PEG} \approx 2.2$ and $f_{PCL} \approx 1.6$. Hence, we assume a strong orientation of the water-insoluble cross-linker at the interface and melt-like dynamics along with collapsed chains for the PCL within the cluster. In ref 82, the RDC values for different molecular weights of linear PCL chains in bulk, reflecting the constrained-Rouse regime of the tube model, are given and range from 200 to 300 Hz, which closely aligns with our value (251 Hz), despite the inherent challenges in comparing these values for different topologies, i.e., comparing constraints imposed by the surrounding network with just entanglements in the melt.

The increase of the RDC value in the PEG region indicates either significant chain stretching, arising from water uptake (explaining the observed equilibrium swelling degree of $Q_{eq} = 4$ despite full incompatibility of PCL/CA and water), or stretching effects arising from the preferential orientation along the normal of the PCL cluster interface. The simulation results (see Figure 6) confirm the strong orientation of the linker group (=chain center) on the cluster surface. Since the simulations do not consider a distinct chemical structure (no

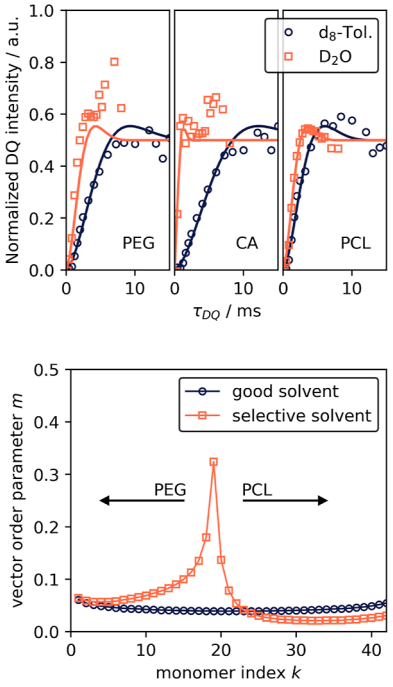

Figure 10. Top: comparison of normalized DQ build-up curves providing the fitted RDC values of CA, PEG, and PCL in ACN swollen in either good (toluene-d_8) or poor solvent (D_2O). Bottom: BFM simulation result of the vector order parameter m for a chain as-prepared and after switching to a selective solvent. k denotes the index in the cross-linked chain, starting at the PCL star core. The observed spike under selective solvent conditions corresponds to the coupling position and its direct surroundings.

Table 3. Site-Specific RDC Values of ACN in Different Solvents at $c = c^*$ from DQ Build-Up Curve Analysis[a]

solvent	RDC_{CA} (Hz)	RDC_{PEG} (Hz)	RDC_{PCL} (Hz)
tol.-d_8	74 ± 2	97 ± 4	149 ± 7
D_2O	748 ± 100	212 ± 20	251 ± 6

[a]Both the value and error of the RDC value for the coupling agent (CA) in D_2O can only be estimated roughly due to the steep initial rise.

distinct interactions) of the linker group, we assume that the observed increase in RDC is only due to the orientation across the interface.

This is confirmed by the vector order parameters m extracted from the simulations (see Figure 10), which are proportional to the RDC values measured by NMR.[50] Both the simulated system and the experimental system were cross-linked at $c = c^*$. Since the interaction parameter between water and PCL is not known, the following comparisons are only of qualitative nature. Upon switching to a selective solvent, m at the position of the coupling agent shows a strong increase (factor 9) from $m_{CA} = 0.041$ to $m_{CA} = 0.343$ (factor 8), which matches the observed increase in the ratio of the RDC values measured by NMR (factor 10) within the given error bars. Additionally, simulations predict an increase in m_{PEG} from $m_{PEG} \approx 0.044$ to $m_{PEG} \approx 0.086$ (average over the chain excluding the coupling position), as well as an increase for the PCL chain order parameter from $m_{PCL} \approx 0.043$ to $m_{PCL} \approx 0.048$. Given that the simulations predict a degree of swelling of the PEG chains of $Q = 5.8$ (whereas $Q = 7$ is observed experimentally), the vector order parameter of the PEG chain

https://doi.org/10.1021/acs.macromol.3c02139
Macromolecules XXXX, XXX, XXX−XXX

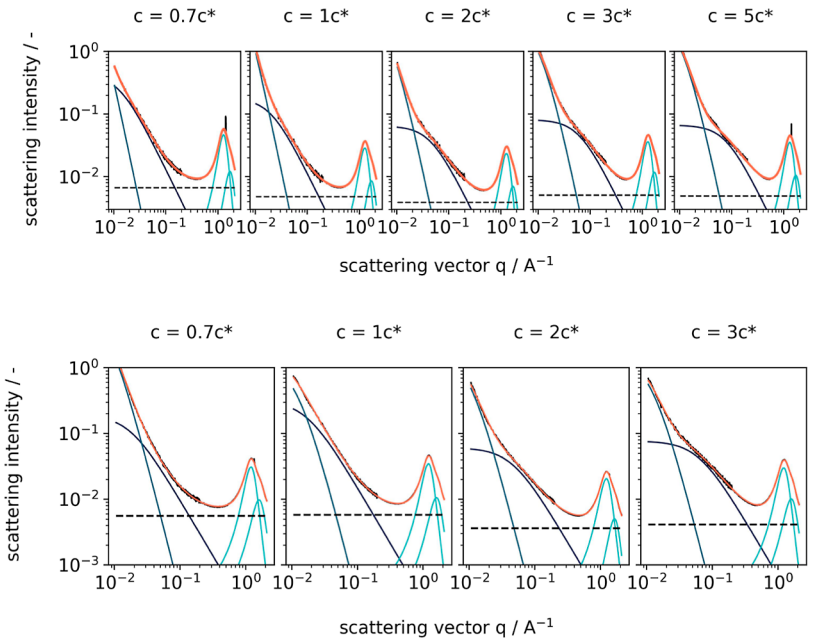

Figure A1. Scattering curves (combined SAXS + WAXS) obtained for different ACNs (top row) and PEG−PEG networks (bottom row) in good solvent (toluene-d_8) at different concentrations. Solid lines are the full fit according to eq 2 as well as the respective components.

is scaled appropriately by a factor of $(7/5.8)^{1/3} \approx 1.06$. All vector order parameters estimated by the simulation are qualitatively reproduced by NMR (PEG: factor 2.0 vs factor 2.2; PCL: factor 1.1 vs factor 1.6). We again remind that systematic distortions may arise from, e.g., significant MAS-induced network deformation, differences in the packing morphology of the PCL clusters, or more complex reasons related to the fine-tuning of the simulations.

CONCLUSIONS

In this study, we examined the structural properties of our PEG−PCL ACNs using various analytical techniques. Specifically, we employed SAXS, PFG NMR, DQ-MAS NMR, and computer simulations to gain insights into the structural characteristics of these networks. We analyzed the SAXS data to determine the Ornstein−Zernike correlation lengths for various preparation concentrations c_{prep}. We were able to extract valuable structural information by comparing the correlation length obtained from SAXS to the hydrodynamic screening length ξ_h from diffusion experiments of two different probe molecules, as well as find qualitative agreement with a scaling exponent expected for semidilute solutions. Significant changes upon drying and reswelling were observed, which simultaneously cause a decrease in both scaling exponent and absolute values of ξ_c. To the best of our knowledge, the influence of postcuring reactions on the topological properties of this type of networks has not been investigated previously and requires further critical examination. To complement the SAXS analysis, we compared the correlation length after drying with a rough estimate of the hydrodynamic screening length obtained from PFG NMR experiments. Surprisingly, despite being fundamentally different methods, these measurements show a good agreement ($\xi \approx 1$ nm).

We also explored the general behavior upon MPS of our networks in a selective solvent. Our findings revealed that MPS can occur despite the topological constraints imposed by the network structure. We observed that the experimentally obtained scattering data remains comparable across different preparation concentrations c_{prep}, suggesting that no large change in the size of the clusters occurs across the investigated range of concentrations despite a changing distribution of connectivity motifs within the network. Therefore, it is concluded that the incompatibility between the solvent and the PCL phase plays a dominant role in driving the chains into nonpreferred conformations with the cross-links acting only as weak constraints that prevent a macroscopic separation into two phases but not directly influencing the overall size distribution of the clusters.

Determining the aggregation number of the PCL clusters from the SAXS data proves challenging without making strong assumptions about the validity of the preferred TS model or alternative assumptions related to the observed peculiarities when applying the KT fitting model. With an assumption on the lattice geometry of the investigated samples, the TS model suggests aggregation numbers in the range of AN = 30−50, whereas the KT model yields a comparable numerical size value but overall inconsistent results. Comparing with computer simulation results, we can narrow the regime toward the lower end. A possible obstruction effect of these nm-sized PCL clusters on probe diffusion is found to be negligible as PFG NMR measurements indicate comparable apparent ξ_h during MPS (stressing again the qualitative nature of these estimates due to limitations of the linear PS probe molecules in a good solvent).

Finally, we compared our findings concerning the local conformational freedom of different moieties obtained through DQ-MAS NMR by examining residual dipolar couplings. We observe a reduced mobility of both PEG and PCL chains (albeit for different reasons, being MPS and chain stretching, respectively), while the linker end group appears to be rather oriented, presumably on the interfaces of the separated domains. These observations are, again, confirmed by BFM simulations.

https://doi.org/10.1021/acs.macromol.3c02139
Macromolecules XXXX, XXX, XXX−XXX

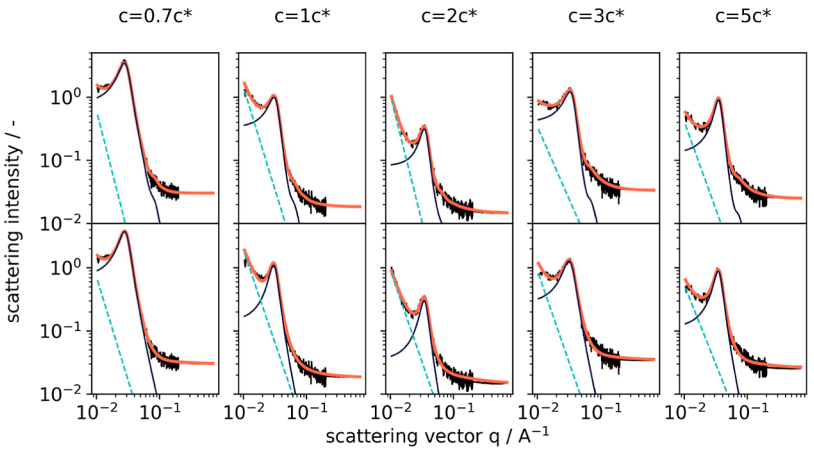

Figure A2. Scattering curves (only SAXS) of ACN at different c_{prep} swollen in water, with fitting results shown as lines. Top: fits of the structural peak (black solid line) to the KT model; bottom: same data, fitted to the TS model.

APPENDIX

Network Strand Length Estimations

The mean-squared end-to-end distance of a PEG chain in bulk can be estimated using the length of the ethylene glycol repeat unit (b = 0.38 nm), the characteristic ratio for long PEG chains (C_∞ = 5), as well as the number of monomers in a star branch (N = 5 kg mol^{-1}/0.044 kg mol^{-1} ≈ 113). All values were taken from refs 83 and 84.

$$\sqrt{\langle R^2 \rangle} = b \cdot \sqrt{NC_\infty} = 9.0 \text{ nm} \quad \text{(A1)}$$

Under the assumption of isotropic swelling, this value can be extrapolated to the end-to-end distance R_Q in a given volume swelling degree Q_V (≈7 for the selective swelling of the PEG chains in water) as follows

$$R_Q = Q_V^{1/3} \cdot \sqrt{\langle R^2 \rangle} = 15.8 \text{ nm} \quad \text{(A2)}$$

However, this estimate neglects any influence of chain stretching induced by topological constraints such as the collapse of the PCL phase, and therefore, this value constitutes only a lower bound. An upper bound for the cluster−cluster separation is given by the contour length

$$l_{contour} = b \cdot N = 40.6 \text{ nm} \quad \text{(A3)}$$

Scattering Curves for All Networks

Figures A1 and A2.

ASSOCIATED CONTENT

Data Availability Statement

All data presented in the figures of this work are available under: zenodo.org/doi/10.5281/zenodo.10012927.

AUTHOR INFORMATION

Corresponding Authors

Lucas Löser − *Institut für Physik—NMR, Martin-Luther-Universität Halle-Wittenberg, 06120 Halle, Germany;* orcid.org/0000-0003-0141-7011; Email: lucas.loeser@physik.uni-halle.de

Kay Saalwächter − *Institut für Physik—NMR, Martin-Luther-Universität Halle-Wittenberg, 06120 Halle, Germany;* orcid.org/0000-0002-6246-4770; Email: kay.saalwaechter@physik.uni-halle.de

Authors

Carolin Bunk − *Leibniz-Institut für Polymerforschung Dresden e.V, 01069 Dresden, Germany;* orcid.org/0000-0002-9760-9255

Reinhard Scholz − *Leibniz-Institut für Polymerforschung Dresden e.V, 01069 Dresden, Germany*

Michael Lang − *Leibniz-Institut für Polymerforschung Dresden e.V, 01069 Dresden, Germany;* orcid.org/0000-0003-3851-6670

Frank Böhme − *Leibniz-Institut für Polymerforschung Dresden e.V, 01069 Dresden, Germany;* orcid.org/0000-0001-6128-4658

Complete contact information is available at: https://pubs.acs.org/10.1021/acs.macromol.3c02139

Notes

The authors declare no competing financial interest.

ACKNOWLEDGMENTS

This work was funded by the German Research Foundation (DFG) through the DFG Research Unit FOR-2811 (project no. 397384169). L.L. thanks the group of Prof. Thomas Thurn-Albrecht (Experimental Polymer Physics, Martin-Luther-Universität Halle-Wittenberg) for generous usage time of their RetroLab-F SAXS setup, the provision of specialized equipment for measurements on wet samples within the vacuum chamber, as well as their extensive and helpful assistance in carrying out the experiments. This includes in particular Martha Schulz for a comprehensive introduction to the scattering methodology and helpful discussions.

REFERENCES

(1) Yoshida, R. Design of Functional Polymer Gels and Their Application to Biomimetic Materials. 2005, http://www.eurekaselect.com/article/558web9.

(2) Kamata, H.; Li, X.; Chung, U.-i.; Sakai, T. Design of Hydrogels for Biomedical Applications. *Adv. Healthcare Mater.* **2015**, *4*, 2360−2374.

(3) Nakayama, D.; Takeoka, Y.; Watanabe, M.; Kataoka, K. Simple and Precise Preparation of a Porous Gel for a Colorimetric Glucose Sensor by a Templating Technique. *Angew. Chem., Int. Ed.* **2003**, *42*, 4197−4200.

(4) Erdodi, G.; Kennedy, J. P. Amphiphilic conetworks: Definition, synthesis, applications. *Prog. Polym. Sci.* **2006**, *31*, 1−18.

(5) Rikkou-Kalourkoti, M.; Patrickios, C. S.; Georgiou, T. K. *6.08—Model Networks and Functional Conetworks*; Elsevier: Amsterdam, 2012; pp 293−308.
(6) Patrickios, C. S.; Georgiou, T. K. Covalent amphiphilic polymer networks. *Curr. Opin. Colloid Interface Sci.* **2003**, *8*, 76−85.
(7) Nicolson, P. C.; Vogt, J. Soft contact lens polymers: an evolution. *Biomaterials* **2001**, *22*, 3273−3283.
(8) Guzman, G.; Es-Haghi, S. S.; Nugay, T.; Cakmak, M. Zero-Order Antibiotic Release from Multilayer Contact Lenses: Nonuniform Drug and Diffusivity Distributions Produce Constant-Rate Drug Delivery. *Adv. Healthcare Mater.* **2017**, *6*, 1600775.
(9) Ozcelik, B.; Brown, K. D.; Blencowe, A.; Ladewig, K.; Stevens, G. W.; Scheerlinck, J.-P. Y.; Abberton, K.; Daniell, M.; Qiao, G. G. Biodegradable and biocompatible poly(ethylene glycol)-based hydrogel films for the regeneration of corneal endothelium. *Adv. Healthcare Mater.* **2014**, *3*, 1496−1507.
(10) Tobis, J.; Boch, L.; Thomann, Y.; Tiller, J. C. Amphiphilic polymer conetworks as chiral separation membranes. *J. Membr. Sci.* **2011**, *372*, 219−227.
(11) Schoenfeld, I.; Dech, S.; Ryabenky, B.; Daniel, B.; Glowacki, B.; Ladisch, R.; Tiller, J. C. Investigations on diffusion limitations of biocatalyzed reactions in amphiphilic polymer conetworks in organic solvents. *Biotechnol. Bioeng.* **2013**, *110*, 2333−2342.
(12) Hanko, M.; Bruns, N.; Tiller, J. C.; Heinze, J. Optical biochemical sensor for determining hydroperoxides in nonpolar organic liquids as archetype for sensors consisting of amphiphilic conetworks as immobilisation matrices. *Anal. Bioanal. Chem.* **2006**, *386*, 1273−1283.
(13) Apostolides, D. E.; Patrickios, C. S.; Sakai, T.; Guerre, M.; Lopez, G.; Améduri, B.; Ladmiral, V.; Simon, M.; Gradzielski, M.; Clemens, D.; Krumm, C.; Tiller, J. C.; Ernould, B.; Gohy, J.-F. Near-Model Amphiphilic Polymer Conetworks Based on Four-Arm Stars of Poly(vinylidene fluoride) and Poly(ethylene glycol): Synthesis and Characterization. *Macromolecules* **2018**, *51*, 2476−2488.
(14) Masaro, L.; Zhu, X. X. Physical models of diffusion for polymer solutions, gels and solids. *Prog. Polym. Sci.* **1999**, *24*, 731−775.
(15) Amsden, B. An Obstruction-Scaling Model for Diffusion in Homogeneous Hydrogels. *Macromolecules* **1999**, *32*, 874−879.
(16) Axpe, E.; Chan, D.; Offeddu, G. S.; Chang, Y.; Merida, D.; Hernandez, H. L.; Appel, E. A. A Multiscale Model for Solute Diffusion in Hydrogels. *Macromolecules* **2019**, *52*, 6889−6897.
(17) Burchard, W. In *Branched Polymers II*; Roovers, J., Ed.; Springer Berlin Heidelberg: Berlin, Heidelberg, 1999; pp 113−194.
(18) Cukier, R. I. Diffusion of Brownian spheres in semidilute polymer solutions. *Macromolecules* **1984**, *17*, 252−255.
(19) Fujiyabu, T.; Li, X.; Chung, U.-i.; Sakai, T. Diffusion Behavior of Water Molecules in Hydrogels with Controlled Network Structure. *Macromolecules* **2019**, *52*, 1923−1929.
(20) Amsden, B. Solute Diffusion within Hydrogels. Mechanisms and Models. *Macromolecules* **1998**, *31*, 8382−8395.
(21) Lust, S. T.; Hoogland, D.; Norman, M. D. A.; Kerins, C.; Omar, J.; Jowett, G. M.; Yu, T.; Yan, Z.; Xu, J. Z.; Marciano, D.; da Silva, R. M. P.; Dreiss, C. A.; Lamata, P.; Shipley, R. J.; Gentleman, E. Selectively Cross-Linked Tetra-PEG Hydrogels Provide Control over Mechanical Strength with Minimal Impact on Diffusivity. *ACS Biomater. Sci. Eng.* **2021**, *7*, 4293−4304.
(22) Guillot, G.; Leger, L.; Rondelez, F. Diffusion of large flexible polymer chains through model porous membranes. *Macromolecules* **1985**, *18*, 2531−2537.
(23) Richbourg, N. R.; Peppas, N. A. High-Throughput FRAP Analysis of Solute Diffusion in Hydrogels. *Macromolecules* **2021**, *54*, 10477−10486.
(24) Fatin-Rouge, N.; Starchev, K.; Buffle, J. Size Effects on Diffusion Processes within Agarose Gels. *Biophys. J.* **2004**, *86*, 2710−2719.
(25) Sun, J.; Lyles, B. F.; Yu, K. H.; Weddell, J.; Pople, J.; Hetzer, M.; Kee, D. D.; Russo, P. S. Diffusion of Dextran Probes in a Self-Assembled Fibrous Gel Composed of Two-Dimensional Arborols. *J. Phys. Chem. B* **2008**, *112*, 29−35.
(26) Colsenet, R.; Söderman, O.; Mariette, F. Pulsed field gradient NMR study of poly(ethylene glycol) diffusion in whey protein solutions and gels. *Macromolecules* **2006**, *39*, 1053−1059.
(27) Matsukawa, S.; Ando, I. Study of Self-Diffusion of Molecules in a Polymer Gel by Pulsed-Gradient Spin-Echo 1H NMR. 2. Intermolecular Hydrogen-Bond Interaction between the Probe Polymer and Network Polymer in N,N-Dimethylacrylamide-Acrylic Acid Copolymer Gel Systems. *Macromolecules* **1997**, *30*, 8310−8313.
(28) Amdursky, N.; Orbach, R.; Gazit, E.; Huppert, D. Probing the Inner Cavities of Hydrogels by Proton Diffusion. *J. Phys. Chem. C* **2009**, *113*, 19500−19505.
(29) Jowkarderis, L.; Van De Ven, T. G. Mesh size analysis of cellulose nanofibril hydrogels using solute exclusion and PFG-NMR spectroscopy. *Soft Matter* **2015**, *11*, 9201−9210.
(30) Amsden, B. G. Hydrogel Mesh Size and Its Impact on Predictions of Mathematical Models of the Solute Diffusion Coefficient. *Macromolecules* **2022**, *55*, 8399−8408.
(31) Zimm, B. H. Dynamics of Polymer Molecules in Dilute Solution: Viscoelasticity, Flow Birefringence and Dielectric Loss. *J. Chem. Phys.* **1956**, *24*, 269−278.
(32) Tsuji, Y.; Li, X.; Shibayama, M. Evaluation of Mesh Size in Model Polymer Networks Consisting of Tetra-Arm and Linear Poly(ethylene glycol)s. *Gels* **2018**, *4*, 50.
(33) Benski, L.; Viran, I.; Katzenberg, F.; Tiller, J. C. Small-Angle X-Ray Scattering Measurements on Amphiphilic Polymer Conetworks Swollen in Orthogonal Solvents. *Macromol. Chem. Phys.* **2021**, *222*, 2000292.
(34) Thünemann, A. F.; Gruber, A.; Klinger, D. Amphiphilic Nanogels: Fuzzy Spheres with a Pseudo-Periodic Internal Structure. *Langmuir* **2020**, *36*, 10979−10988.
(35) Yang, X.; Zhang, H.; Zhao, J.; Liu, Y.; Zhang, Z.; Liu, Y.; Yan, X. Multiscale supramolecular polymer network with microphase-separated structure enabled by host-guest self-sorting recognitions. *Chem. Eng. J.* **2022**, *450*, 138135.
(36) Kitiri, E. N.; Varnava, C. K.; Patrickios, C. S.; Voutouri, C.; Stylianopoulos, T.; Gradzielski, M.; Hoffmann, I. Double-networks based on interconnected amphiphilic "in−out" star first polymer conetworks prepared by RAFT polymerization. *J. Polym. Sci., Part A: Polym. Chem.* **2018**, *56*, 2161−2174.
(37) Rikkou-Kalourkoti, M.; Kitiri, E. N.; Patrickios, C. S.; Leontidis, E.; Constantinou, M.; Constantinides, G.; Zhang, X.; Papadakis, C. M. Double Networks Based on Amphiphilic Cross-Linked Star Block Copolymer First Conetworks and Randomly Cross-Linked Hydrophilic Second Networks. *Macromolecules* **2016**, *49*, 1731−1742.
(38) Ulrich, S.; Sadeghpour, A.; Rossi, R. M.; Bruns, N.; Boesel, L. F. Wide Range of Functionalized Poly(N-alkyl acrylamide)-Based Amphiphilic Polymer Conetworks via Active Ester Precursors. *Macromolecules* **2018**, *51*, 5267−5277.
(39) Teubner, M.; Strey, R. Origin of the scattering peak in microemulsions. *J. Chem. Phys.* **1987**, *87*, 3195−3200.
(40) Kinning, D. J.; Thomas, E. L. Hard-sphere interactions between spherical domains in diblock copolymers. *Macromolecules* **1984**, *17*, 1712−1718.
(41) Zeng, D.; Ribbe, A.; Hayward, R. C. Anisotropic and Interconnected Nanoporous Materials from Randomly End-Linked Copolymer Networks. *Macromolecules* **2017**, *50*, 4668−4676.
(42) Zhang, X.; Kyriakos, K.; Rikkou-Kalourkoti, M.; Kitiri, E. N.; Patrickios, C. S.; Papadakis, C. M. Amphiphilic single and double networks: a small-angle X-ray scattering investigation. *Colloid Polym. Sci.* **2016**, *294*, 1027−1036.
(43) Krakovský, I.; Szekély, N. Small-angle neutron scattering study of nanophase separated epoxy hydrogels. *J. Non-Cryst. Solids* **2010**, *356*, 368−373.
(44) Guo, H.; Mussault, C.; Brûlet, A.; Marcellan, A.; Hourdet, D.; Sanson, N. Thermoresponsive Toughening in LCST-Type Hydrogels with Opposite Topology: From Structure to Fracture Properties. *Macromolecules* **2016**, *49*, 4295−4306.
(45) Truong, V.; Blakey, I.; Whittaker, A. K. Hydrophilic and Amphiphilic Polyethylene Glycol-Based Hydrogels with Tunable

https://doi.org/10.1021/acs.macromol.3c02139
Macromolecules XXXX, XXX, XXX−XXX

Degradability Prepared by "Click" Chemistry. *Biomacromolecules* **2012**, *13*, 4012−4021.
(46) Hiroi, T.; Kondo, S.; Sakai, T.; Gilbert, E. P.; Han, Y.-S.; Kim, T.-H.; Shibayama, M. Fabrication and Structural Characterization of Module-Assembled Amphiphilic Conetwork Gels. *Macromolecules* **2016**, *49*, 4940−4947.
(47) Kamata, H.; Akagi, Y.; Kayasuga-Kariya, Y.; Chung, U.-i.; Sakai, T. Nonswellable" Hydrogel Without Mechanical Hysteresis. *Science* **2014**, *343*, 873−875.
(48) Krumm, C.; Konieczny, S.; Dropalla, G. J.; Milbradt, M.; Tiller, J. C. Amphiphilic Polymer Conetworks Based on End Group Cross-Linked Poly(2-oxazoline) Homo- and Triblock Copolymers. *Macromolecules* **2013**, *46*, 3234−3245.
(49) Bunk, C.; Löser, L.; Fribiczer, N.; Komber, H.; Jakisch, L.; Scholz, R.; Voit, B.; Seiffert, S.; Saalwächter, K.; Lang, M.; Böhme, F. Amphiphilic Model Networks Based on PEG and PCL Tetra-arm Star Polymers with Complementary Reactivity. *Macromolecules* **2022**, *55*, 6573−6589.
(50) Lang, M.; Scholz, R.; Löser, L.; Bunk, C.; Fribiczer, N.; Seiffert, S.; Böhme, F.; Saalwächter, K. Swelling and Residual Bond Orientations of Polymer Model Gels: The Entanglement-Free Limit. *Macromolecules* **2022**, *55*, 5997−6014.
(51) Prakash, J. R. Universal dynamics of dilute and semidilute solutions of flexible linear polymers. *Curr. Opin. Colloid Interface Sci.* **2019**, *43*, 63−79.
(52) Newville, M.; et al. *Lmfit/Lmfit-py: 1.0.3*; Zenodo, 2021.
(53) Debye, P.; Bueche, A. M. Scattering by an Inhomogeneous Solid. *J. Appl. Phys.* **1949**, *20*, 518−525.
(54) Ornstein, L. S. Accidental deviations of density and opalescence at the critical point of a single substance. *Proc. Akad. Sci.* **1914**, *17*, 793.
(55) Yan, T.; Schröter, K.; Herbst, F.; Binder, W. H.; Thurn-Albrecht, T. Unveiling the molecular mechanism of self-healing in a telechelic, supramolecular polymer network. *Sci. Rep.* **2016**, *6*, 32356.
(56) McDermott, A. G.; Budd, P. M.; McKeown, N. B.; Colina, C. M.; Runt, J. Physical aging of polymers of intrinsic microporosity: a SAXS/WAXS study. *J. Mater. Chem. A* **2014**, *2*, 11742−11752.
(57) Hiei, Y.; Ohshima, I.; Hara, M.; Seki, T.; Hoshino, T.; Takeoka, Y. Shrinking rates of polymer gels composed of star-shaped polymers of N-isopropylacrylamide and dimethylacrylamide copolymers: the effect of dimethylacrylamide on the crosslinking network. *Soft Matter* **2022**, *18*, 5204−5217.
(58) Percus, J. K.; Yevick, G. J. Analysis of Classical Statistical Mechanics by Means of Collective Coordinates. *Phys. Rev.* **1958**, *110*, 1−13.
(59) Wertheim, M. S. Exact Solution of the Percus-Yevick Integral Equation for Hard Spheres. *Phys. Rev. Lett.* **1963**, *10*, 321−323.
(60) Thiele, E. Equation of State for Hard Spheres. *J. Chem. Phys.* **1963**, *39*, 474−479.
(61) Mordvinkin, A.; Suckow, M.; Böhme, F.; Colby, R. H.; Creton, C.; Saalwächter, K. Hierarchical Sticker and Sticky Chain Dynamics in Self-Healing Butyl Rubber Ionomers. *Macromolecules* **2019**, *52*, 4169−4184.
(62) Stejskal, E. O.; Tanner, J. E. Spin Diffusion Measurements: Spin Echoes in the Presence of a Time-Dependent Field Gradient. *J. Chem. Phys.* **1965**, *42*, 288−292.
(63) Price, W. S. Pulsed-Field Gradient Nuclear Magnetic Resonance as a Tool for Studying Translational Diffusion: Part 1. Basic Theory. *Concepts Magn. Reson.* **1997**, *9*, 299−336.
(64) Rubinstein, M.; Colby, R. H. *Polymer Physics*; Oxford University Press: Oxford, 2007.
(65) Phillies, G. D. J. Universal scaling equation for self-diffusion by macromolecules in solution. *Macromolecules* **1986**, *19*, 2367−2376.
(66) Wallace, M.; Adams, D. J.; Iggo, J. A. Analysis of the mesh size in a supramolecular hydrogel by PFG-NMR spectroscopy. *Soft Matter* **2013**, *9*, 5483−5491.
(67) Nedelcu, S.; Sommer, J.-U. Single chain dynamics in polymer networks: A Monte Carlo study. *J. Chem. Phys.* **2009**, *130*, 204902.
(68) de Gennes, P. G. Reptation of a Polymer Chain in the Presence of Fixed Obstacles. *J. Chem. Phys.* **1971**, *55*, 572−579.
(69) De Gennes, P.-G. *Scaling Concepts in Polymer Physics*; Cornell University Press, 1979.
(70) Hohwy, M.; Jakobsen, H. J.; Edén, M.; Levitt, M. H.; Nielsen, N. C. Broadband dipolar recoupling in the nuclear magnetic resonance of rotating solids: A compensated C7 pulse sequence. *J. Chem. Phys.* **1998**, *108*, 2686−2694.
(71) Lange, F.; Schwenke, K.; Kurakazu, M.; Akagi, Y.; Chung, U.-i.; Lang, M.; Sommer, J.-U.; Sakai, T.; Saalwächter, K. Connectivity and Structural Defects in Model Hydrogels: A Combined Proton NMR and Monte Carlo Simulation Study. *Macromolecules* **2011**, *44*, 9666−9674.
(72) Chassé, W.; Valentín, J. L.; Genesky, G. D.; Cohen, C.; Saalwächter, K. Precise dipolar coupling constant distribution analysis in proton multiple-quantum NMR of elastomers. *J. Chem. Phys.* **2011**, *134*, 044907.
(73) Naumova, A.; Agudelo, D. C.; Villar, M. A.; Vega, D. A.; Valentin, J. L.; Saalwächter, K. Microscopic State of Polymer Network Chains upon Swelling and Deformation. *Macromolecules* **2019**, *52*, 5042−5053.
(74) Matsunaga, T.; Sakai, T.; Akagi, Y.; Chung, U.-i.; Shibayama, M. SANS and SLS Studies on Tetra-Arm PEG Gels in As-Prepared and Swollen States. *Macromolecules* **2009**, *42*, 6245−6252.
(75) Fleischer, G.; Zgadzai, O. E.; Skirda, V. D.; Maklakov, A. I. Self-diffusion of polystyrene in solution 1. Experimental results of the NMR pulsed field gradient technique. *Colloid Polym. Sci.* **1988**, *266*, 201−207.
(76) Augé, S.; Schmit, P.-O.; Crutchfield, C. A.; Islam, M. T.; Harris, D. J.; Durand, E.; Clemancey, M.; Quoineaud, A.-A.; Lancelin, J.-M.; Prigent, Y.; Taulelle, F.; Delsuc, M.-A. NMR Measure of Translational Diffusion and Fractal Dimension. Application to Molecular Mass Measurement. *J. Phys. Chem. B* **2009**, *113*, 1914−1918.
(77) Morris, E. R.; Cutler, A. N.; Ross-Murphy, S. B.; Rees, D. A.; Price, J. Concentration and shear rate dependence of viscosity in random coil polysaccharide solutions. *Carbohydr. Polym.* **1981**, *1*, 5−21.
(78) Tirtaatmadja, V.; Dunstan, D. E.; Boger, D. V. Rheology of dextran solutions. *J. Non-Newtonian Fluid Mech.* **2001**, *97*, 295−301.
(79) Braeckmans, K.; Peeters, L.; Sanders, N. N.; De Smedt, S. C.; Demeester, J. Three-Dimensional Fluorescence Recovery after Photobleaching with the Confocal Scanning Laser Microscope. *Biophys. J.* **2003**, *85*, 2240−2252.
(80) Fetters, L. J.; Hadjichristidis, N.; Lindner, J. S.; Mays, J. W. Molecular Weight Dependence of Hydrodynamic and Thermodynamic Properties for Well-Defined Linear Polymers in Solution. *J. Phys. Chem. Ref. Data* **1994**, *23*, 619−640.
(81) Köhler, W.; Rosenauer, C.; Rossmanith, P. Holographic grating study of mass and thermal diffusion of polystyrene/toluene solutions. *Int. J. Thermophys.* **1995**, *16*, 11−21.
(82) Kurz, R.; Schulz, M.; Scheliga, F.; Men, Y.; Seidlitz, A.; Thurn-Albrecht, T.; Saalwächter, K. Interplay between Crystallization and Entanglements in the Amorphous Phase of the Crystal-Fixed Polymer Poly(*ε*-caprolactone). *Macromolecules* **2018**, *51*, 5831−5841.
(83) Lee, H.; Venable, R. M.; MacKerell, A. D.; Pastor, R. W. Molecular Dynamics Studies of Polyethylene Oxide and Polyethylene Glycol: Hydrodynamic Radius and Shape Anisotropy. *Biophys. J.* **2008**, *95*, 1590−1599.
(84) Gerstl, C.; Schneider, G. J.; Pyckhout-Hintzen, W.; Allgaier, J.; Willbold, S.; Hofmann, D.; Disko, U.; Frielinghaus, H.; Richter, D. Chain Conformation of Poly(alkylene oxide)s Studied by Small-Angle Neutron Scattering. *Macromolecules* **2011**, *44*, 6077−6084.

https://doi.org/10.1021/acs.macromol.3c02139
Macromolecules XXXX, XXX, XXX−XXX